Dynamic Modeling and Experimental Analysis of a Two-Ray Undulatory Fin Robot

Michael Sfakiotakis, John Fasoulas, and Roza Gliva

Abstract— Bio-inspired undulatory fin propulsion holds considerable potential for endowing robotic underwater vehicles with low-speed manoeuvrability and stable station-keeping. Robotic fins typically comprise a number of serially arranged and individually actuated "fin rays", interconnected by a membrane-like flexible surface. Propulsive forces are generated by the propagation of a traveling wave along the mechanism, via appropriately timed ray oscillations. The present paper describes a dynamic model for an elementary two-ray fin system, analyzed as a standard robot mechanism with additional contributions arising from the elastic deformation of the flexible membrane and from the hydrodynamic forces. The model's main aspects, particularly with regard to the hydrodynamic effects, are explored via simulation studies, as well as via experiments with a robotic prototype. The developed model can serve a number of purposes towards optimizing the mechanical design, the control strategies, and the propulsive efficacy of robotic undulatory fins.

Index Terms— Undulatory fin propulsion, Biologically-inspired robots, Underwater robots.

I. INTRODUCTION

Undulatory fin propulsion, inspired by the swimming of knifefish, rays, and cuttlefish [1], holds considerable potential for endowing aquatic vehicles with precision manoeuvrability and stable station-keeping, in the context of applications such as underwater structure inspection and maintenance. The motivation stems mainly from the thrust vectoring capacity of undulatory fins, and from the ability to integrate them into rigid-body vehicles. Other postulated advantages, compared to propellers, include increased energy efficiency, reduced sediment disruption and stealth operation.

Similar to actinopterygian fish fins, robotic fins are typically comprised by a series of individually actuated "fin rays", interconnected via a flexible "membrane" sheet (Fig. 1). Appropriately timed oscillations of the rays lead to the propagation of a propulsion-generating wave along the mechanism. Most of the developed robotic fins have considerably fewer rays (typically 8 to 12) than their biological counterparts (featuring as many as 300 rays). The rays are usually driven by R/C servomotors [2]–[9], although alternative actuation methods have also been proposed [10]–[14]. The membrane is made from materials such as silicone rubber, latex, and stretchable fabric.

Developing computational models to predict the thrust of undulatory fins presents significant challenges due to the complex hydrodynamic interactions between the continuously flexing fin surface and the aquatic environment, which result in forces being generated in all three (axial, normal, and lateral) directions. Early efforts to analytically estimate the axial thrust and efficiency of undulating fin propulsion have applied the actuator-disc method [15], waving plate theory extended by blade element analysis [16], and elongated body theory [17]. An alternative approach, adopted by a number of more recent studies, is based on integrating over the fin surface the hydrodynamic forces, approximated by a simplified fluid drag model, which act on infinitesimal propulsive elements [18]–[21]. Sophisticated numerical flow solvers may help provide a more complete picture for the thrust generation mechanisms of undulatory fins, as demonstrated by the very significant insights gained from a number of recent CFD studies in this area [22], [23]. However, since these methods are very computationally intensive, it is difficult to use them for investigating an extensive kinematic parameter space. Moreover, CFD models cannot be directly employed for control purposes.

In preceding work, we have developed and verified a model for the dynamics of an elementary two-ray mechanism operating in air, focusing on the effect of the elastic membrane on the rays' actuation torques [24]. In the current paper, we extend this model by incorporating the fin's hydrodynamics, through which propulsive forces are generated, via the above simplified fluid drag model. Our formulation of the model takes into explicit account the spatial discretization of the undulatory wave, as it considers the actual shape of the membrane, rather than the idealized one. The underlying motivation relates to developing a robotics-oriented dynamic model of undulatory fin mechanisms, currently lacking in the literature, applicable to analyzing and optimizing their mechanical design, control, and propulsive performance.
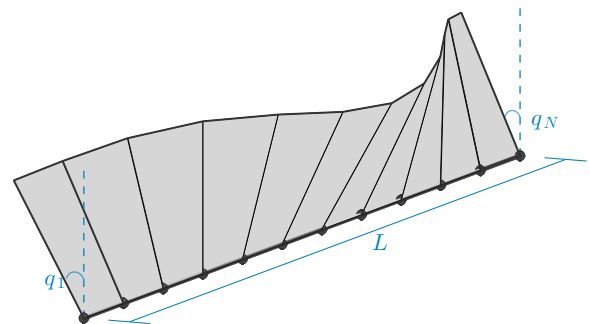
Fig. 1: Schematic of an undulatory fin mechanism, comprised of N actuated rigid rays, equally distributed along the fin's baseline.

Section II of the paper overviews the kinematics of undulatory fin mechanisms. Section III presents the developed dynamic model of an elementary two-ray system submerged in water. Simulation results, highlighting the model's main aspects, are provided in Section IV-B. Finally, Section V describes the setup and obtained results from a series of experiments to assess the validity of the proposed model.

II. UNDULATORY FIN KINEMATICS

The propagation of a basic uni-directional wave along the N-ray fin mechanism of Fig. 1, can be obtained by imposing the following angular trajectories for the fin ray joints q_i:

$$q_i(t) = A \sin\left(2\pi f t - (i-1)\phi_0\right), \ i = 1...N, \quad (1)$$

with the corresponding joint velocities being:

$$\dot{q}_i(t) = 2\pi f A \cos\left(2\pi f t - (i-1)\phi_0\right), \quad (2)$$

where f and A denote respectively the frequency and amplitude of the rays' oscillation, while ϕ_0 is the inter-ray phase shift. When $\phi_0 > 0$ (respectively, $\phi_0 < 0$), the undulatory wave propagates towards the Nth ray (resp., the 1st ray), while for $\phi_0 = 0$ the fin oscillates as a single plate surface (i.e., there in no undulation). The number of waves along the fin is $w_n = |\phi_0| (N-1)/2\pi$, indicating that, as N is reduced, $|\phi_0|$ must increase in order to maintain a desired number of waves. Evidently, the number of rays in the fin determines how closely the spatial discretization of the wave approximates a true sine, particularly as w_n is increased.

As will become apparent from the analysis in the following Sections, a key variable of the system are the inter-ray separation angles $q_i(t) - q_{i+1}(t)$ (where $i = 1, ..., N-1$). For the traveling wave formulation (1), it can be shown that:

$$q_i(t) - q_{i+1}(t) = \Theta \cdot \text{sgn}(\phi_0) \cos\left(2\pi f t + \frac{\phi_0}{2} - i\phi_0\right), \quad (3)$$

where $\Theta = A\sqrt{2(1-\cos\phi_0)}$, i.e., the maximum separation angle increases with the inter-ray phase shift, as well as with the rays' maximum angular deflection. It can also be shown that, when $q_i - q_{i+1} = \pm\Theta$, then $\dot{q}_i = \dot{q}_{i+1}$ and $q_i = -q_{i+1}$. Conversely, when $q_i - q_{i+1} = 0$, then $\dot{q}_i = -\dot{q}_{i+1}$.

III. MODELING AND SYSTEM DYNAMICS

In this Section, we present a dynamic model of a basic two-ray fin robot, that also takes into account the effects of the membrane's elasticity and hydrodynamic forces.

A. System description

The system is modeled as a three-link robot mechanism comprised of two rigid rays (links l_1 and l_2 in Fig. 2), attached via single-d.o.f. active revolute joints (q_1 and q_2) to an interconnecting rigid link l_0. The rays are coupled through an elastic membrane, while a passive prismatic joint q_0, whose axis coincides with those of the revolute joints, allows translation of the whole mechanism along the z-axis of the body frame $\{O\}$. Gravity is assumed to act parallel to the x-axis of the inertial frame $\{P\}$, shown in Fig. 2.
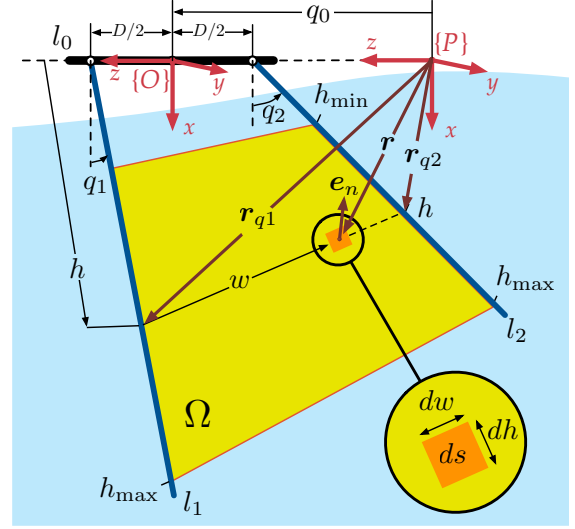

Fig. 2: Schematic diagram of the two-ray system.

The membrane, which is considered massless, is immersed in water and attached span-wise along the two rays, as indicated in Fig. 2. It has a nominally rectangular shape, with an overall span H, a natural length ℓ and a nominal thickness ζ, while $h_{\min}$ and $h_{\max} = h_{\min} + H$ denote respectively the proximal and distal mounting distance from the ray's joint. The modulus of elasticity and the Poisson ratio of the membrane are denoted as E and v, respectively. The parameter $\alpha = D/\ell$, where D is the distance between the two revolute joints, denotes the nominal (i.e., for $q_1 = q_2$) tension level of the membrane. We assume here that $\alpha \geq 1$, i.e., the membrane is tautly attached to the fin rays, in order to withstand hydrodynamic loads without buckling.

B. Dynamics of the system outside the water

Denoting as $\boldsymbol{q} = [\,q_0 \ q_1 \ q_2\,]^T$ the generalized coordinates of the system, the dynamic equation of the non-submerged two-ray mechanism can be written as [24]:

$$\boldsymbol{M}\ddot{\boldsymbol{q}} + \boldsymbol{B}\dot{\boldsymbol{q}} + \boldsymbol{G}(\boldsymbol{q}) + \boldsymbol{K}_c\text{sgn}(\dot{\boldsymbol{q}}) + \boldsymbol{\Gamma}(q_1 - q_2) = \boldsymbol{\tau}, \quad (4)$$

where $\boldsymbol{M} = \text{diag}(M_0, M_1, M_2)$ is the mass matrix of the system, with $M_i = m_i\left(\frac{l_i}{2}\right)^2 + I_{zi}$ (for $i = 1, 2$) being a positive scalar that includes the mass m_i, the length l_i, and the moment of inertia I_{zi} of the i-th ray. In addition, $M_0 := m_0 + m_1 + m_2$ is the total mass of the mechanism, where m_0 is the mass of the interconnecting link with length l_0 and moment of inertia I_{z0}. The generalized gravity force vector, which affects only the motion of the rays, is $\boldsymbol{G}(\boldsymbol{q}) = [\,0 \ g_1\sin q_1 \ g_2\sin q_2\,]^T$, where $g_i = \frac{l_i}{2}m_i g$ ($i = 1, 2$, while g denotes the acceleration of gravity). In addition, $\boldsymbol{B} = \text{diag}(b_0, b_1, b_2)$ and $\boldsymbol{K}_c = \text{diag}(k_{c0}, k_{c1}, k_{c2})$ are positive definite matrices with b_i, k_{ci} representing the viscous friction coefficient and the Coulomb friction for the i-th joint.

The term $\boldsymbol{\Gamma}(q_1 - q_2) \in \Re^{3\times 1}$ in (4) represents the generalized force of the joints q_i due to the elastic deformation of the membrane, obtained as [24]:

$$\boldsymbol{\Gamma}(q_1 - q_2) = [\,0 \ \tau_{\Gamma,1} \ \tau_{\Gamma,2}\,]^T, \quad (5)$$

where the joint torques $\tau_{\mathrm{r},i}$ $(i=1,2)$ are:

$$\tau_{\mathrm{r},i}=(-1)^{i+1}\sin(q_1-q_2)E\zeta\left(\Lambda(h_{\max})-\Lambda(h_{\min})\right),\quad(6)$$

with

$$\Lambda(x)=\frac{x^3\alpha}{3D}\left(1+v\frac{8-3\alpha\sqrt{\kappa^2+1}}{4}\right)-\quad(7)$$
$$-\frac{D^2}{2p^3}(\sqrt{\kappa^4+\kappa^2}-\sinh^{-1}\kappa)\left(1+v\frac{4+\alpha^2}{4}\right)$$
$$\alpha=D/\ell,\ p=\sqrt{2(1-\cos(q_1-q_2))},\ \text{and}\ \kappa=\frac{x}{D}p.$$

Finally, the generalized force vector $\boldsymbol{\tau}=\begin{bmatrix}0&\tau_1&\tau_2\end{bmatrix}^T$ in (4) incorporates the control input torques τ_1,τ_2 generated by the actuators at the revolute joints.

C. Underwater system dynamics

Here, we extend the dynamic model to consider the case of the fin moving underwater, assuming, for simplicity, that link l_0 lies above the water surface. In order to model the interactions of the immersed fin with it's surrounding fluid, we adopt a simplified quasi-steady approach, applicable to large Reynolds-number flow regimes, that ignores secondary effects of the fluid's motion [18]–[21]. Under these assumptions, the hydrodynamic force is obtained by integrating, over the fin's surface, the drag forces arising from the pressure differentials created by the movement of infinitesimal fin surface elements.

Hydrodynamic force: Let Ω be a given snapshot of the skew quadrilateral fin surface, which depends on the separation angle q_1-q_2. The position $\boldsymbol{r}$ of any surface element $ds=dh\cdot dw$, parametrized in terms of it's length-wise and span-wise coordinates (respectively denoted as w and h), can by obtained from the position vectors $\boldsymbol{r}_{q_i}$ (see Fig. 2) as follows:

$$\boldsymbol{r}=\boldsymbol{r}_{q_1}+\frac{\boldsymbol{r}_{q_2}-\boldsymbol{r}_{q_1}}{\|\boldsymbol{r}_{q_2}-\boldsymbol{r}_{q_1}\|}w\ ,\quad(8)$$

where, denoting as $c_i=\cos(q_i)$ and $s_i=\sin(q_i)$,

$$\boldsymbol{r}_{q_i}=\begin{bmatrix}hc_i&hs_i&q_0+(-1)^{i+1}\dfrac{D}{2}\end{bmatrix}^T\ i=1,2\ .\quad(9)$$

Substituting for (9) in (8) eventually yields:

$$\boldsymbol{r}=\begin{bmatrix}c_1h+\dfrac{(c_2-c_1)hw}{w_{\max}}&s_1h+\dfrac{(s_2-s_1)hw}{w_{\max}}&q_0+\dfrac{D}{2}-\dfrac{Dw}{w_{\max}}\end{bmatrix}$$

where $w_{\max}=\sqrt{2h^2(1-\cos(q_1-q_2))+D^2}\geq D$ represents the length of the fin strip at height h (for the given separation angle q_1-q_2), obtained as the distance $\|\boldsymbol{r}_{q_2}-\boldsymbol{r}_{q_1}\|$.

Furthermore, defining $\boldsymbol{r}_h=\frac{\partial\boldsymbol{r}}{\partial h}$ and $\boldsymbol{r}_w=\frac{\partial\boldsymbol{r}}{\partial w}$, the normal vector $\boldsymbol{e}_n$ for each surface element (see Fig. 2) can be shown to be obtained as:

$$\boldsymbol{e}_n=\frac{\boldsymbol{r}_h\times\boldsymbol{r}_w}{\|\boldsymbol{r}_h\times\boldsymbol{r}_w\|}=\frac{D}{\delta}\begin{bmatrix}s_1(\bar{w}-1)-s_2\bar{w}\\-c_1(\bar{w}-1)+c_2\bar{w}\\-\sin(q_1-q_2)\frac{h}{D}\end{bmatrix},\quad(10)$$

where we have introduced the normalized length-wise coordinate $\bar{w}=\frac{w}{w_{\max}}$, whose range is $0\leq\bar{w}\leq1$, while

$$\delta=\sqrt{2D^2\bar{w}(\bar{w}-1)(1-\cos(q_1-q_2))+h^2\sin^2(q_1-q_2)+D^2}.$$

According to the simplified fluid drag model [18]–[21], the hydrodynamic force, acting perpendicular to an individual surface element ds, is approximated as:

$$\boldsymbol{f}_n=\frac{\boldsymbol{F}_n}{ds}=-\frac{1}{2}\rho C_n\boldsymbol{e}_n v_n^2\mathrm{sgn}(v_n)\ ,\quad(11)$$

where $v_n=\boldsymbol{e}_n^T\dot{\boldsymbol{r}}$ denotes the velocity component normal to the surface element, C_n is the drag coefficient and ρ is the fluid density. After a series of algebraic and trigonometric manipulations, v_n can be written in terms of h and $\bar{w}$ as:

$$v_n=\frac{Dh}{\delta}\left(\dot{q}_1-\frac{\sin(q_1-q_2)\dot{q}_0}{D}+(1-\cos(q_1-q_2))(\dot{q}_1+\dot{q}_2)\bar{w}^2+\right.$$
$$\left.+(\cos(q_1-q_2)(\dot{q}_1+\dot{q}_2)-2\dot{q}_1)\bar{w}\right)\ .\quad(12)$$

The overall hydrodynamic force $\boldsymbol{F}_N=\begin{bmatrix}F_x&F_y&F_z\end{bmatrix}^T$ of the fin may then be obtained by integrating the contributions from all the infinitesimal surfaces:

$$\boldsymbol{F}_N(\boldsymbol{q},\dot{\boldsymbol{q}})=\int_{h_{\min}}^{h_{\max}}\int_0^{w_{\max}}\boldsymbol{f}_n dwdh=\int_{h_{\min}}^{h_{\max}}\int_0^1\boldsymbol{f}_n d\bar{w}dh\ .\quad(13)$$

The three components F_x, F_y, and F_z (expressed in the robot's body frame $\{O\}$) of $\boldsymbol{F}_N$ are respectively termed as *heave*, *sway* and *surge* force. Although very complex, analytical expressions can be derived, with the aid of symbolic computation software, for the three components of the $\boldsymbol{f}_n$ vector. These are then numerically integrated, as per (13), to obtain $\boldsymbol{F}_N$ for specific values of the parameters involved.

Dynamics of the immersed fin: The hydrodynamic contributions on the system dynamics are obtained via the corresponding generalized joint forces $\boldsymbol{\Phi}(\boldsymbol{q},\dot{\boldsymbol{q}})\in\Re^{3\times1}$ for the robot mechanism, from:

$$\boldsymbol{\Phi}(\boldsymbol{q},\dot{\boldsymbol{q}})=\int_{h_{\min}}^{h_{\max}}\int_0^1\boldsymbol{J}^T(-\boldsymbol{f}_n)d\bar{w}dh\ ,\quad(14)$$

where the Jacobian (expressed in terms of h and $\bar{w}$)

$$\boldsymbol{J}=\frac{\partial\boldsymbol{r}}{\partial\boldsymbol{q}}=\begin{bmatrix}0&0&1\\-s_1h(1-\bar{w})&c_1h(1-\bar{w})&0\\-s_2h\bar{w}&c_2h\bar{w}&0\end{bmatrix}^T,\quad(15)$$

relates the velocity $\dot{\boldsymbol{r}}$ of the surface element with the joint velocities $\dot{\boldsymbol{q}}$, i.e., $\dot{\boldsymbol{r}}=\boldsymbol{J}\dot{\boldsymbol{q}}$. Taking into account (13)-(15), the hydrodynamic contributions can be written as:

$$\boldsymbol{\Phi}(\boldsymbol{q},\dot{\boldsymbol{q}})=\begin{bmatrix}-F_z&\tau_{\Phi,1}&\tau_{\Phi,2}\end{bmatrix}^T,\quad(16)$$

i.e., the surge component F_z of the hydrodynamic force acts directly on the prismatic joint q_0 of the mechanism, while, as indicated by (13), (15) the hydrodynamic torques arising at the fin ray joints (denoted as $\tau_{\Phi,1}$, $\tau_{\Phi,2}$), only depend on

the heave F_x and sway F_y components. The three elements of $\boldsymbol{\Phi}(\boldsymbol{q},\dot{\boldsymbol{q}})$ can be calculated with the same methodology adopted for the calculation of $\boldsymbol{F}_N$.

By incorporating (14) in (4), we derive the following dynamic equation of the submerged fin mechanism:

$$\boldsymbol{L}(\ddot{\boldsymbol{q}},\dot{\boldsymbol{q}},\boldsymbol{q})+\boldsymbol{\Gamma}(q_1-q_2)+\boldsymbol{\Phi}(\boldsymbol{q},\dot{\boldsymbol{q}})=\boldsymbol{\tau}, \quad (17)$$

where $\boldsymbol{L}=\begin{bmatrix}\tau_{L,0} & \tau_{L,1} & \tau_{L,2}\end{bmatrix}^T$ consists of the robot's inertia, friction and generalized gravity force:

$$\boldsymbol{L}(\ddot{\boldsymbol{q}},\dot{\boldsymbol{q}},\boldsymbol{q})=\boldsymbol{M}\ddot{\boldsymbol{q}}+\boldsymbol{B}\dot{\boldsymbol{q}}+\boldsymbol{K}_c\mathrm{sgn}(\dot{\boldsymbol{q}})+\boldsymbol{G}(\boldsymbol{q}), \quad (18)$$

while the term $\boldsymbol{\Gamma}(q_1-q_2)$ in (17) is due to the membrane's deformation and $\boldsymbol{\Phi}(\boldsymbol{q},\dot{\boldsymbol{q}})$ due to the hydrodynamics.

The developed model (17) can be easily extended to consider multiple serially-arranged two-ray units, in order to study the dynamics of a complete fin mechanism. We also note that, unlike other efforts [18]–[21], our formulation of the fluid drag model contributions takes explicitly into account the actual shape (a changing skew quadrilateral) of the membrane segment between the rays, rather than its idealized sinusoidal shape. This affords a more accurate description for the overall system, and enables the study of the effect of the various practical fin parameters (number of rays, inter-ray spacing etc.) on the generalized forces of the mechanism. Moreover, since the hydrodynamics are introduced in (17) in generic terms of $\boldsymbol{q}$, $\dot{\boldsymbol{q}}$, it is possible to consider and study propulsion generation through different (e.g., non sinusoidal) motion profiles for the rays.

IV. SIMULATION STUDIES

This Section presents simulations highlighting various aspects of the developed model, particularly with regard to the hydrodynamic effects.

A. Inverse dynamics analysis

An inverse dynamics approach is employed, imposing a specific motion profile $\boldsymbol{q}$, $\dot{\boldsymbol{q}}$, $\ddot{\boldsymbol{q}}$ for the mechanism's joints to solve for the corresponding actuating forces and torques. In particular, we consider initially the case of a stationary (i.e, constrained from translating) undulating fin mechanism, by setting $q_0(t)=\dot{q}_0(t)=\ddot{q}_0(t)=0$ for the prismatic joint, while specifying from (1), (2) the motion of the fin ray revolute joints q_1, q_2. The required actuation torques for the latter are then obtained from (17) as $\tau_i=\tau_{L,i}+\tau_{\Gamma,i}+\tau_{\Phi,i}$, where $\tau_{\Gamma,i}$, $\tau_{\Phi,i}$ and $\tau_{L,i}$ encompass the terms described respectively from (5), (14) and (18).

The fin ray parameters were specified as $m_i=0.01$kg, $l_i=0.12$m, $I_{zi}=72\cdot10^{-6}$kg/m^2, $b_i=0.02$Nms/rad, and $k_{ci}=0.001$Nm $(i=1,2)$. The membrane's parameters were $h_{\min}=0$, $h_{\max}=0.12$m, $D=0.08$m, $\alpha=1$, $v=0.5$, and $E\zeta=360$N/m, while the hydrodynamic parameters were set as $\rho=1022$kg/m^3 and $C_n=2.8$. The surface integrals that appear in (13), (14) were numerically evaluated using the `quad2d` function of Matlab.

Indicative results from one such simulation run are provided in Fig. 3, while the accompanying video provides a

corresponding 3d animation to help visualize the motion of the mechanism and the development of the generated hydrodynamic force. Regarding the latter, Fig. 3b indicates that the axial (surge) component F_z oscillates at twice the undulation frequency. Since F_z is always positive, it's time-averaged value will be non-zero, thereby generating a net propulsive force. The vertical (heave) component F_x also oscillates at a frequency $2f$, but has a zero mean value. Finally, the lateral (sway) component F_y oscillates at the same frequency as the rays, with a zero mean value. The temporal evolution of F_x, F_y, F_z is closely linked to that of the rays' separation angle q_1-q_2 (cf. Fig. 3a): All three components equal zero when $q_1-q_2=0$, while the peaks for F_z and F_y occur when $q_1-q_2=\pm\Theta$ (the heave component is $F_x=0$ at these instances).

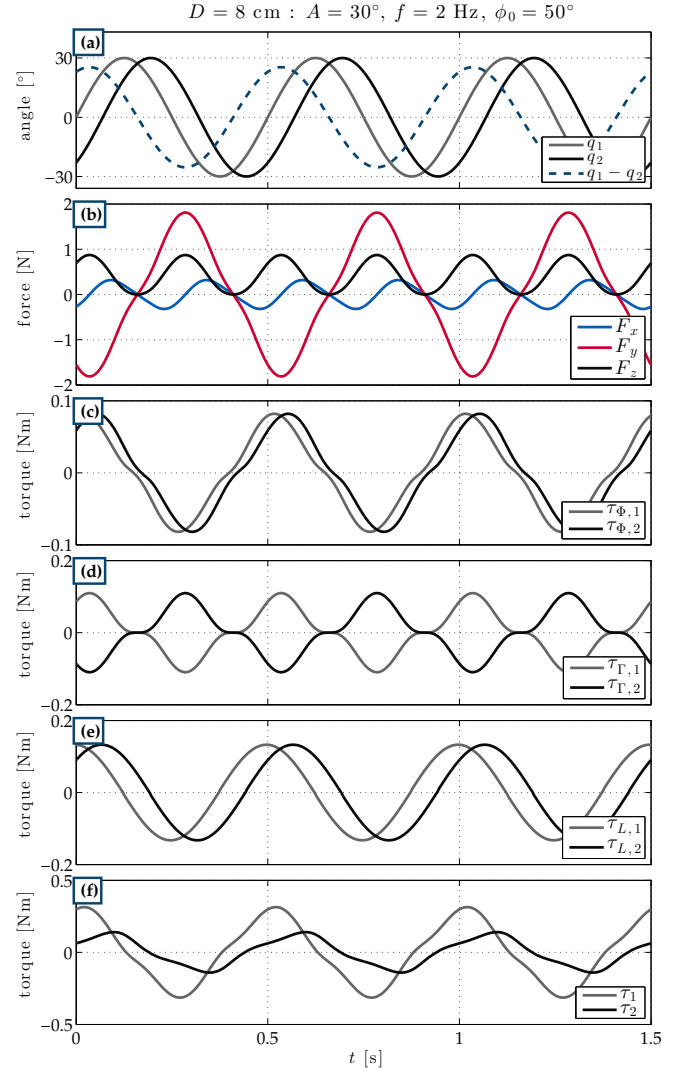Regarding the actuation torques corresponding to the hy-

Fig. 3: Indicative simulation results for a stationary two-ray fin: (a) motion profile of the rays, (b) hydrodynamic force components, (c) fin ray joint torques due to the hydrodynamic loads, (d) fin ray joint torques due to the elastic membrane, (e) fin ray joint torques due to inertia, gravity and friction, and (f) total fin ray joint torques.
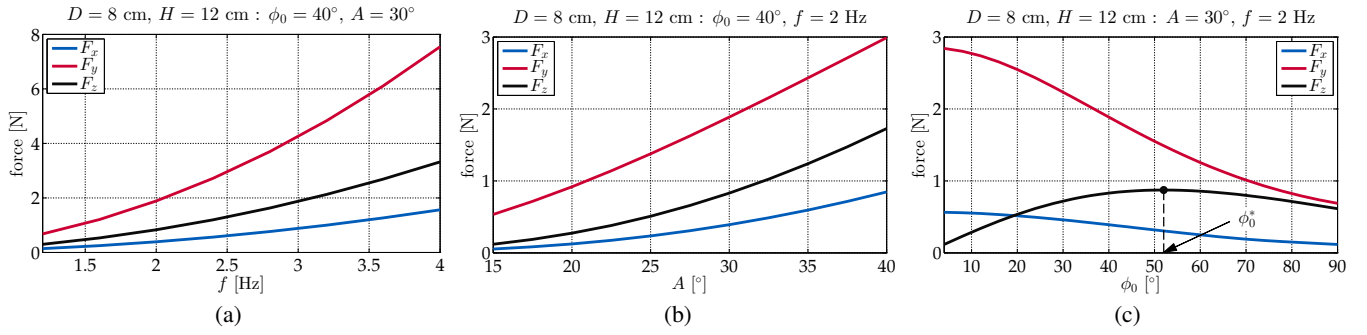
Fig. 4: Simulation results: Maximum instantaneous values of the three components of the hydrodynamic force (cf. Fig. 3b), shown against (a) the rays' oscillation frequency, (b) the rays' oscillation amplitude, and (c) the inter-ray phase shift.

drodynamic loads at the mechanism's revolute joints (Fig. 3c), it is noted that the delay of $\tau_{\Phi,2}$ with respect to $\tau_{\Phi,1}$ is different than the inter-ray phase shift ϕ_0, while $\tau_{\Phi,1}=\tau_{\Phi,2}$ when $q_1-q_2=\pm\Theta$. The torques due to the elastic deformation of the membrane (Fig. 3d) are also maximized when $q_1-q_2=\pm\Theta$. The joint torques combinedly arising from the inertial, friction and gravity terms (Fig. 3e), indicate that $\tau_{L,1}=\tau_{L,2}$ when $q_1-q_2=\pm\Theta$. Finally, the total required actuation torques τ_1 and τ_2, corresponding to the sum of the above torque components, are provided in Fig. 3f. It is worth noting that, due to the effect of the elastic membrane, the torque requirements for the joint of the ray leading the motion (in this case, q_1) are higher than those of the other joint (in this case, q_2).

B. Parametric analysis

Fig. 4 shows the results of a parametric investigation for the effect of the undulation parameters f, A, and ϕ_0 on the amplitude (i.e., maximum instantaneous value, cf. Fig. 3b) of the three hydrodynamic force components. In particular, Fig. 4a shows that all three components increase quadratically with the rays' oscillation frequency (assuming the rest of the parameters to remain constant). The results shown in Fig. 4b indicate that the amplitude of both the surge (F_z) and heave (F_x) components increases in an approximately quadratic manner with the rays' maximum angular deflection, while the increase of the sway (F_y) component is more gradual. Finally, Fig. 4c indicates that the amplitude of the heave and sway forces decreases with the inter-ray phase shift. By contrast, there is an optimum, intermediate, value of the inter-ray phase shift (denoted as ϕ_0^*) that maximizes the amplitude (and, hence, also the average value) of the surge component. This is in agreement with the results of prior experimental and numerical studies [2], [10], [19], [23].

Focusing into this particular aspect, Fig. 5a shows the variation of the average axial force $\bar{F}_z$ as a function of ϕ_0, for different values of A, with constant f=2Hz. It can be seen that the optimal phase shift ϕ_0^* moves towards smaller values for increasing A. This trend is consistent with the findings of our experimental investigations with an 8-ray robotic fin [2]. An additional series of simulations considered the effect of varying the phase shift ϕ_0, as well as the inter-
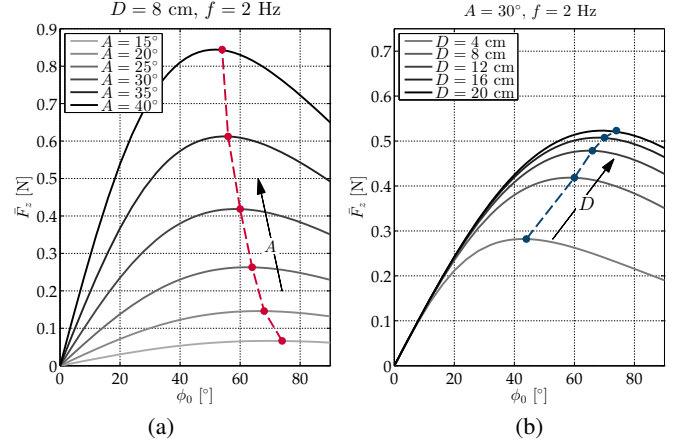

Fig. 5: Simulation results: Variance of the average surge force with respect to the inter-ray phase shift, for different values of (a) the rays' angular amplitude, and (b) the inter-ray spacing. In both plots, the dashed line indicates the change of the optimal phase shift ϕ_0^*.

ray distance D (and, hence, the overall area and aspect ratio of the membrane), while retaining constant the amplitude and frequency of the rays' oscillation. The results, shown in Fig. 5b, indicate that the optimal phase shift ϕ_0^* moves towards higher values for increasing D.

Finally, Fig. 6 shows the maximum fin ray joint torques arising from the hydrodynamics and from the membrane deformation, with respect to the inter-ray phase shift. The results illustrate the increase of $\tau_{\Phi,i}$ as ϕ_0 is reduced, i.e., as larger volumes of water are shed laterally by the fin motions. By contrast, $\tau_{\Gamma,i}$ increases considerably with ϕ_0, reflecting the increased loads for stretching further the elastic membrane. Since the membrane is considered purely elastic, $\tau_{\Gamma,i}$ is independent of the wave frequency f, unlike $\tau_{\Phi,i}$. Therefore, the relative contribution of the hydrodynamic torques increases with the wave frequency (cf. Fig. 6a and Fig. 6b), particularly for small values of ϕ_0.

The results presented in this Section highlight how the developed model may be utilized in the design of undulatory fin mechanisms, providing guidelines for the anticipated thrust forces, as well as for the associated torque requirements to help in the specification of the fin ray actuators.
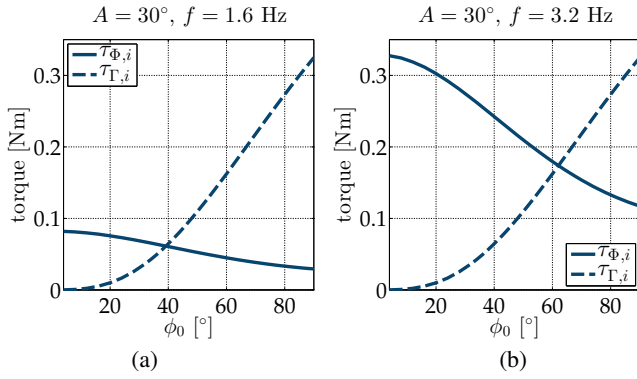
Fig. 6: Simulation results: Variance of the maximum instantaneous fin ray torque requirements arising from the hydrodynamic loads (solid line) and from the membrane deformation (dashed line), as a function of the inter-ray phase shift, for two different values of the wave frequency f.

V. EXPERIMENTAL MODEL VALIDATION

This Section describes a prototype two-ray fin mechanism, along with a series of experiments to validate the developed computational model, the main focus being the characteristics of the surge force generated by the fin.

A. Two-ray fin prototype

The experimental testbed involves a fin mechanism with two independently actuated fin ray modules, interconnected by a sheet of elastic membrane. A CAD drawing of the mechanism is provided in Fig. 7, where the inset shows the components comprising the fin ray modules. In order to ensure a high degree of rigidity (as per the model's assumptions), each ray is made from two 2.0mm thick stainless steel flat plates (height: 17.6cm, width: 0.6cm), with screws used to secure the membrane sheet in-between them. The ray's revolute joint is actuated by a 12V digital servomotor (*Herkulex DRS-201, Dongbu Robot Co.*), which receives commands and provides feedback regarding the ray's position (obtained by an internal potentiometer) over a multidrop full duplex asynchronous serial bus. The inter-spacing of the two fin ray modules can be adjusted so as to accommodate membrane specimens of different length. The membrane segments used in the present study were obtained from a 0.275mm-thick sheet of green-colored silicone rubber, with a modulus of elasticity E=1.3GPa [24].

The two-ray fin is mounted on a carriage equipped with 4 grooved roller bearings, constrained to only slide axially along a linear guide over the water tank where the tests take place, whose dimensions are 210 x 90 x 50 cm. The total mass of the fin mechanism (including the carriage assembly) is M=2.42kg. A 50N-capacity load-cell (*SMT1, Interface Inc.*), mounted on the linear guide, is employed to measure the surge component of the force generated by the fin undulations. The total current drawn by the servos is monitored using a Hall-effect sensor (*ACS714, Allegro MicroSystems LLC*). The setup also includes a laser distance sensor (*efector200-01D100, Ifm Gmbh*), placed on the edge of the tank, that is used to track the motion of the carriage during tests involving self-propulsion of the mechanism.

Fig. 8 depicts the fin's control architecture. The high level controller, running on a host PC as a multi-rate Simulink model under Real Time Windows Target, implements a Central Pattern Generator (CPG) [2] to calculate on-line the desired angular trajectories of the rays with smooth startup transients. These are transmitted to the low level control unit, where an *Arduino Mega2560* microcontroller generates the corresponding command packages to the servomotors. The reverse path is employed for relaying to the host PC feedback for the servos' actual positions. Concurrent with the servo control loop, which runs at a 100Hz rate, the sensors' analog outputs are processed via first-order anti-aliasing RC filters (with a 50Hz cutoff frequency), and are then digitized at a 1kHz rate by a 16-bit data acquisition card (*NI-6221, National Instruments*) inside the PC.

B. Experimental results

The experiments presented here were focused on measurement of the axial force generated by in-place fin undulations. To this end, the mechanism was attached to the load cell (Fig. 9), thereby imposing that $q_0(t)=\dot{q}_0(t)=\ddot{q}_0(t)=0$. Data were collected for two different membrane specimens, with the same height H=14cm and different lengths (ℓ=7cm and ℓ=9cm). In both cases, the membrane was mounted on the rays at $h_{\min}$=3.4cm and $h_{\max}$=17.4cm, while the spacing D between the two ray modules was set equal to the membrane length ℓ, in order to have α=1, in accordance with the model's assumptions.

Each run commenced with both fin rays in the vertical position. Subsequently, the CPG network running at the workstation PC was initiated, to generate the reference trajectories q_1^d and q_2^d for the two rays, with a desired oscillation amplitude A, oscillation frequency f, and phase shift ϕ_0 according to the parameter set under investigation. Data regarding the instantaneous axial force F_z and overall current consumption i_m, as well as the rays' actual joint angles q_1 and q_2, were then collected over the experiment's duration, specified each time to equal 10 undulation periods.
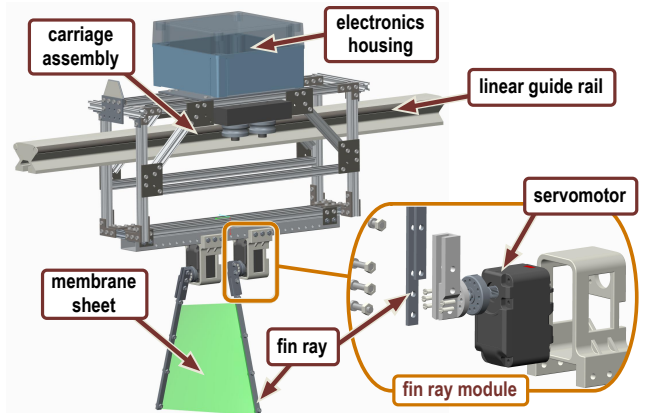

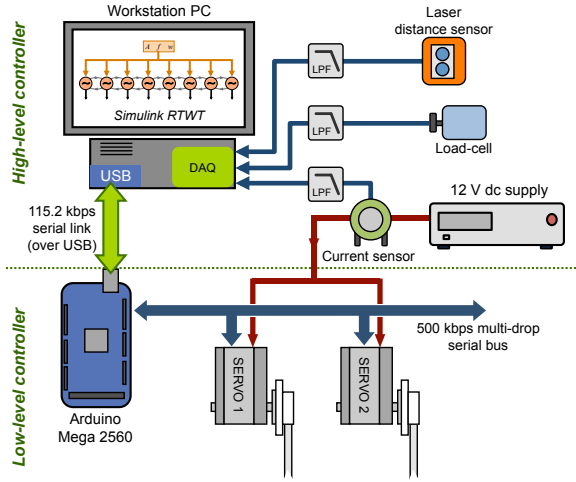Fig. 7: CAD drawing of the experimental two-ray fin prototype.

Fig. 8: The fin mechanism control architecture.

Before commencing the next experiment, sufficient time was allowed for the water in the tank to settle.

The acquired data for F_z and i_m were post-processed by a digital 10-th order low-pass zero-phase Butterworth filter to remove sensor noise. In addition, estimates for the rays' angular velocities $\dot{q}_1$ and $\dot{q}_2$ were obtained by numerical differentiation of the servomotors' positions q_1 and q_2. These $\boldsymbol{q}$ and $\dot{\boldsymbol{q}}$ sequences, from each experiment run, were then input to the computational model, to generate from (13) a simulated sequence for the axial thrust force F_z. For these simulations, the model's parameters were specified to correspond to those of the experimental testbed.

Indicative results from one such test run are provided in Fig. 10. The upper graph shows the actual (rather than the desired) angular position of the mechanism's two rays, along with the separation angle, where the initial transient (lasting about 2.5s) is due to the CPG. The temporal evolution of the post-processed axial force F_z from the load-cell (denoted by the thick red line) along with the corresponding simulation results (thin black line), are shown in Fig. 10b. Finally, Fig. 10c plots the instantaneous current consumption i_m of the servomotors during the experiment. Overall, it can be seen that the model captures effectively the variations of the

Fig. 9: The experimental setup during measurements of the axial force generated by the two-ray fin prototype undulating in-place.
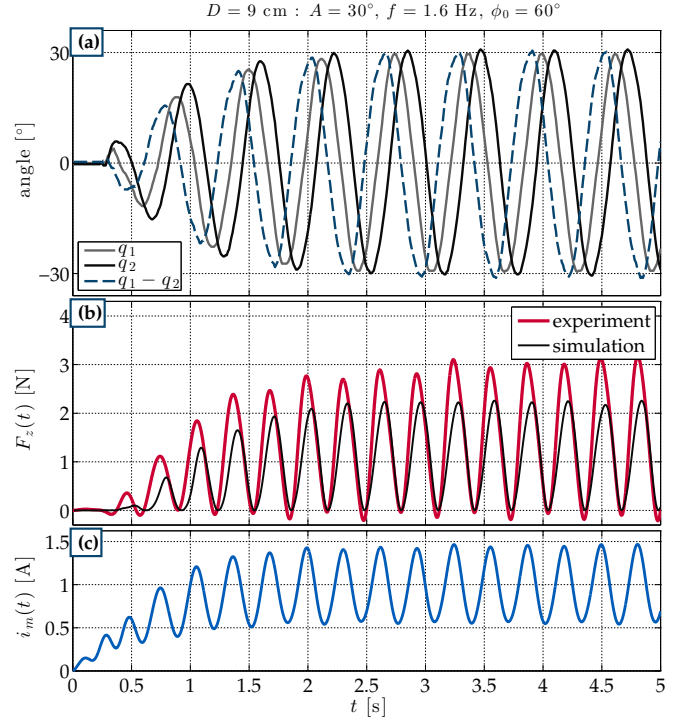

Fig. 10: Indicative results from the axial thrust measurement experiments.

generated thrust, oscillating at twice the fin frequency with a non-zero mean value. The data also confirm the predictions of the model regarding the timing of F_z with respect to that of the separation angle. It is noted that the temporal fluctuation of the servomotors' current demand (Fig. 10c) is also synchronized with that of q_1-q_2.

Fig. 11 provides a summary of the steady-state average axial thrust $\bar{F}_z$ generated by the fin mechanism, as a function of the inter-ray phase shift, over a range of frequencies and with a nominal (desired) oscillation amplitude $A=30°$, for the two membrane specimens. It can be seen that the simulation results (dashed lines) exhibit considerable quantitative, as well as qualitative, agreement with the experimental data (solid lines with markers). In particular, we note that the model captures effectively the optimal phase shift ϕ_0^*, even for those cases where the quantitative match is not very good (e.g., for $f=1.6$Hz). In addition, the experimental data confirm the shift of ϕ_0^* towards higher values for the longer membrane segment. A number of factors may have contributed in the quantitative discrepancies, primarily related to the inherent simplifications of the fluid drag model, but also to limitations of the experimental setup (e.g., hydrodynamic interactions due to the finite dimensions of the test tank).

Finally, it is worth noting that, assuming an appropriate combination of the wave kinematic parameters is selected, the developed prototype is capable of delivering considerable amounts of thrust, despite having only two rays. Indeed, in a series of self-propulsion tests (sample runs are provided in the accompanying video), the prototype attained a maximum average steady-state velocity of around 30cm/s (as estimated via the distance sensor data).
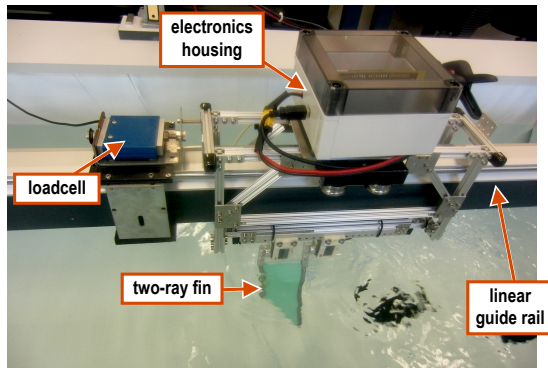
(a) results for $D=7$cm, with $A=30°$
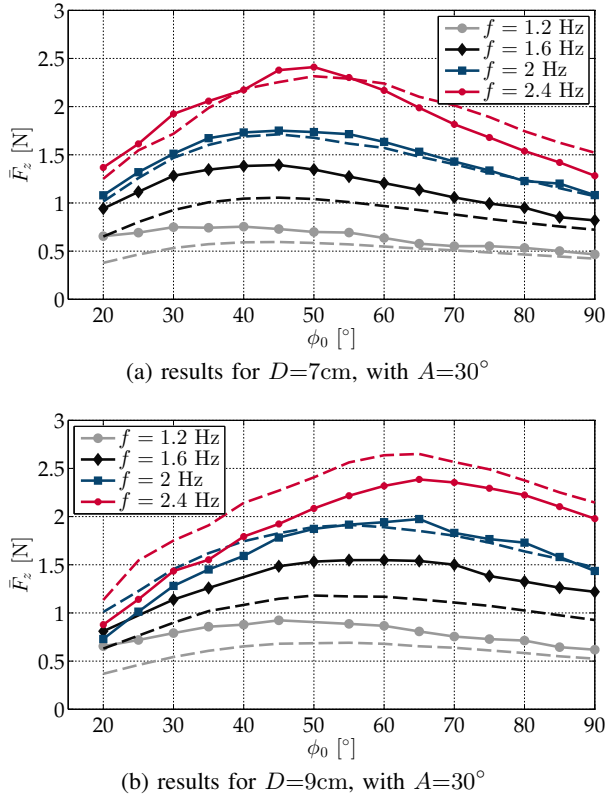

(b) results for $D=9$cm, with $A=30°$

Fig. 11: Average surge force as a function of the inter-ray phase shift, at four different wave frequencies, for the two membrane specimens. In both graphs, experimental data are denoted by solid lines with markers, while the dashed lines denote the values obtained via the computational model.

VI. CONCLUSIONS

We have presented a dynamic model for a two-ray robotic undulatory fin, which incorporates contributions from the hydrodynamic interactions and the membrane deformation, as well as those from gravity, friction and inertia of the rays. Our simulation and experimental results indicate that the main effects of hydrodynamics are captured effectively, despite the simplifications of the adopted fluid drag model. As an example of the possible uses of these computational tools, we note that a computed-torque control strategy, based on the developed model, is currently under development, to improve the trajectory tracking of the rays. Future work will also consider extensions to multi-ray fin mechanisms, unconstrained underwater motion, and path planning.

ACKNOWLEDGMENT

REFERENCES

[1] M. Sfakiotakis, D. Lane, and J. Davies, "Review of fish swimming modes for aquatic locomotion," *IEEE J. Oceanic Eng.*, vol. 24, no. 2, pp. 237–252, 1999.

[2] M. Sfakiotakis, J. Fasoulas, M. M. Kavoussanos, and M. Arapis, "Experimental investigation and propulsion control for a bio-inspired robotic undulatory fin," *Robotica*, vol. 33, no. 5, pp. 1062–1084, 2015.

[3] H. Xie and L. Shen, "Dynamic analysis on the bionic propulsor imitating undulating fin of aquatic animals," in *Proc. IEEE Int. Conf. Rob. Biomim.*, pp. 268–273, 2008.

[4] T. Hu, L. Shen, L. Lin, and H. Xu, "Biological inspirations, kinematics modeling, mechanism design and experiments on an undulating robotic fin inspired by *Gymnarchus niloticus*," *Mech. Mach. Theory*, vol. 44, no. 3, pp. 633 – 645, 2009.

[5] L. Shang, S. Wang, M. Tan, and X. Dong, "Motion control for an underwater robotic fish with two undulating long-fins," in *Proc. IEEE Int. Conf. on Decision and Control (CDC'09)*, pp. 6478–6483, 2009.

[6] M. Epstein, J. E. Colgate, and M. A. MacIver, "Generating thrust with a biologically-inspired robotic ribbon fin," in *Proc. IEEE/RSJ Int. Conf. Intell. Robots Syst.*, pp. 2412–2417, 2006.

[7] M. M. Rahman, S. Sugimori, H. Miki, R. Yamamoto, Y. Sanada, and Y. Toda, "Braking performance of a biomimetic squid-like underwater robot," *J. Bion. Eng.*, vol. 10, no. 3, pp. 265–273, 2013.

[8] D. Simons, M. M. C. Bergers, S. Henrion, J. I. J. Hulzenga, R. W. Jutte, W. M. G. Pas, M. Van Schravendijk, T. G. A. Vercruyssen, and A. P. Wilken, "A highly versatile autonomous underwater vehicle with biomechanical propulsion," in *Proc. OCEANS'09*, pp. 1–6, 2009.

[9] K. Low, "Modelling and parametric study of modular undulating fin rays for fish robots," *Mech. Mach. Theory*, vol. 44, no. 3, pp. 615–632, 2009.

[10] O. Curet, N. Patankar, G. Lauder, and M. MacIver, "Mechanical properties of a bio-inspired robotic knifefish with an undulatory propulsor," *Bioinsp. & Biomim.*, vol. 6, no. 2, p. 026004, 2011.

[11] M. Sfakiotakis, D. M. Lane, and B. J. Davies, "An experimental undulating-fin device using the parallel bellows actuator," in *Proc. IEEE Int. Conf. Robot. Autom.*, pp. 2356–2362, 2001.

[12] H. Xu, L. Lin, D. Zhang, and H. Xie, "Experimental study on the bionic undulate thruster driven by a hydraulic system," in *Proc. IEEE Int. Conf. Rob. Biomim.*, pp. 441–444, 2009.

[13] K. Takagi, M. Yamamura, Z.-W. Luo, M. Onishi, S. Hirano, K. Asaka, and Y. Hayakawa, "Development of a rajiform swimming robot using ionic polymer artificial muscles," in *Proc. IEEE/RSJ Int. Conf. Intell. Robots Syst.*, pp. 1861–1866, 2006.

[14] Y.-H. Zhang, J.-H. He, J. Yang, S.-W. Zhang, and K. Low, "A computational fluid dynamics (CFD) analysis of an undulatory mechanical fin driven by shape memory alloy," *Int. J. Autom. Comput.*, vol. 3, pp. 374–381, 2006.

[15] R. W. Blake, "Median and paired fin propulsion," in *Fish Biomechanics* (P. W. Webb and D. Weihs, eds.), pp. 214–247, New York: Praeger Publishers, 1983.

[16] T. L. Daniel, "Forward flapping flight from flexible fins," *Can. J. Zool.*, vol. 66, no. 3, pp. 630–638, 1988.

[17] M. J. Lighthill and R. W. Blake, "Biofluiddynamics of balistiform and gymnotiform locomotion. 1. Biological background, and analysis by elongated-body theory," *J. Fluid Mech.*, vol. 212, pp. 183–207, 1990.

[18] M. Epstein, J. E. Colgate, and M. A. MacIver, "A biologically inspired robotic ribbon fin," in *Proc. IEEE/RSJ Int. Conf. Intell. Robots Syst.*, (Edmonton, Canada), 2005.

[19] H. Xie and D. Yin, "Dynamics and initial experiments of bionic undulating fish fin," in *Chinese Automation Congress (CAC), 2013*, pp. 643–650, Nov 2013.

[20] S. Sefati, I. D. Neveln, M. A. MacIver, E. S. Fortune, and N. J. Cowan, "Counter-propagating waves enhance maneuverability and stability: a bio-inspired strategy for robotic ribbon-fin propulsion," in *Proc. IEEE/RAS-EMBS Int. Conf. Biomed. Robot. Biomechatron.*, pp. 1620–1625, 2012.

[21] S. Sefati, I. D. Neveln, E. Roth, T. Mitchell, J. B. Snyder, M. A. MacIver, E. S. Fortune, and N. J. Cowan, "Mutually opposing forces during locomotion can eliminate the tradeoff between maneuverability and stability," *Proc. Natl. Acad. Sci. Usa*, 2013.

[22] I. D. Neveln, R. Bale, A. P. S. Bhalla, O. M. Curet, N. A. Patankar, and M. A. MacIver, "Undulating fins produce off-axis thrust and flow structures," *J. Exp. Biol.*, vol. 217, pp. 201–213, 2014.

[23] A. Shirgaonkar, O. Curet, N. Patankar, and M. MacIver, "The hydrodynamics of ribbon-fin propulsion during impulsive motion," *J. Exp. Biol.*, vol. 211, no. 21, pp. 3490–3503, 2008.

[24] M. Sfakiotakis and J. Fasoulas, "Development and experimental validation of a model for the membrane restoring torques in undulatory fin mechanisms," in *Proc. IEEE Medit. Conf. on Control and Automation (MED'14)*, (Palermo, Italy), pp. 1540–1546, 2014.